Characterization of Ion Cluster Dissociation in Ion Electrospray Thrusters Using Time of Flight Mass Spectrometry

IEPC-2022-225

Presented at the 37th International Electric Propulsion Conference
Massachusetts Institute of Technology, Cambridge, MA, USA
June 19-23, 2022

Catherine E. Miller[1]
Middlebury College, Middlebury, VT, 05753, USA

Time of flight mass spectrometry is used to measure the dissociation rates of positive EMI-BF_4 dimers as a function of the electric field strength within the acceleration region of a single emitter ionic liquid ion source. The experimentally measured rates are compared with existing analytical and numerical models. The effects of ionic liquid temperature, source current, and source potential on the dissociation rates are also investigated. The ion source was operated at a range of source potentials (1720V −2020V) and ionic liquid temperatures (30°C – 110°C). The experimentally measured mean lifetimes of positive EMI-BF_4 dimers range from $0.04 - 2.5$ μs, depending on the source potential, ionic liquid temperature, and acceleration region electric field strength. The mean lifetimes decrease with increasing electric field strength and increasing ionic liquid temperature. The experimentally measured rates are not in agreement with model predictions, which may be a consequence of the dimer mean temperature decreasing as the dimer population evolves through the acceleration region.

I. Introduction

Microsatellites need propulsion systems in order to meet various space mission objectives. Required thrust levels are on the order of tens to hundreds of microNewtons for main propulsion and attitude control. Without micropropulsion, CubeSats have fewer capabilities and are limited to shorter mission durations [1]. Mature electric propulsion technologies, such as gridded ion engines and Hall effect thrusters, suffer from reduced performance when scaled down to sizes and power levels compatible with microsatellites [2]. This has necessitated the development of new electric propulsion technologies more well-suited for microsatellite applications. Ion electrospray propulsion is a promising micropropulsion technology that has been under development for over a decade [3, 4]. Ion electrospray thrusters generate ion beams through the application of strong electric fields to the ionic liquid propellant. Ionic liquids are composed of molecular cations and anions, which are field-evaporated and accelerated to high speeds by the electric field. The ion beams emanating from ion electrospray thrusters are composed of single ions as well as clusters of ions [3]. The ion clusters vary in size and tend to dissociate rapidly and in large fractions [5–10]. This process of dissociation is often referred to in the literature as fragmentation. Thruster performance is reduced by the dispersity of the ion beam as well as the dissociation of ion clusters within the thruster [8]. However, low energy ions, which are products of dissociation, are necessary for spacecraft neutralization [11].

The fundamental physics of ion cluster dissociation in ion electrospray thrusters has yet to be completely characterized. Experiments have demonstrated that different ionic liquid propellants produce different fractions of dissociated clusters, suggesting that the ion cluster dissociation rates depend on the molecular composition of the ions [8, 9]. Additionally, cluster dissociation rates may depend on other conditions, such as the presence of an external electric field [9, 10, 12]. Within the *acceleration region* of an ion electrospray thruster, the electric field varies by several orders of magnitude, with the strongest field at the emission site. The region outside the thruster has zero electric field and is referred to in this work as the *field-free region*. The field-free region (FFR) dissociation rates of dimers, a type of ion cluster described in Section II, were recently measured using a retarding potential analyzer (RPA) for several ionic liquids [9, 12]. It was found that the population of dimers exponentially decays, through the process of dissociation, at a constant rate

[1]Visiting Assistant Professor, Department of Physics, cm2@middlebury.edu

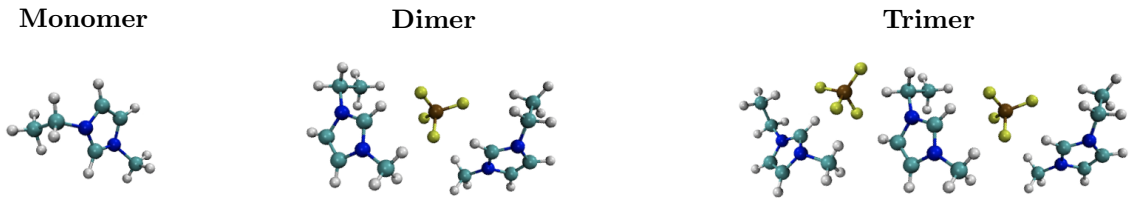

Fig. 1 EMI-BF_4 positive ion species. [8]

in the FFR. The dissociation rates within the acceleration region were also probed, but not thoroughly characterized, with an RPA [12]. Experimental measurements and analytical models suggest that the dimer population decreases linearly with electric potential throughout most of the acceleration region, [6, 8, 12] except near the emission site. The dissociation rates in the acceleration region are of particular interest since dissociation in this region strongly affects thruster performance.

Analytical and numerical models have been used to investigate the effect of an external electric field on ion cluster dissociation [9, 10, 13, 14]. Previous work suggests that ion cluster dissociation can be modeled as an activated process and that the presence of an external electric field lowers the energy barrier for dissociation [15–17]. An image potential model (IPM) [10, 12, 16] and a dipole model [10] both predict that the dissociation rates in the low-field section of the acceleration region should be approximately constant with respect to the electric field strength. These two analytical models were recently compared with molecular dynamics (MD) simulations of EMI-BF_4 ion clusters in the presence of an external electric field [10]. It was found that the analytical models do not adequately capture the physics of cluster dissociation in the high-field section of the acceleration region where the electric field strength exceeds 10^8 V/m. Near the emission site, the analytical models predict a rapid increase in dissociation rate with increasing electric field, whereas the MD simulations show that the dissociation rate levels off as the field strength increases. Experimental measurements of the dissociation rates in the acceleration region, particularly in the high-field region, are necessary to better characterize this process.

II. Ion Cluster Dissociation in Ionic Liquid Ion Sources

A. Ionic Liquid Ion Sources

Ionic liquid ion sources (ILIS) produce pure ion beams from ionic liquid propellant [3]. Ionic liquids are molten salts at room temperature that consist of molecular, or sometimes atomic, cations and anions. Electric fields, with strengths in excess of 10^9 V/m, can be used to field-evaporate ions from the liquid. Once evaporated, these ions are accelerated by the electric field and exit the source at high speeds. ILIS's can be operated in either positive or negative polarity, which results in sprays of positively charged ions or negatively charged ions, respectively. Consider a positively charged ion beam generated by an EMI-BF_4 ILIS[a]. The ion beam consists of several ion species including single ions, called *monomers* (which in this case are EMI^+ ions) and ion clusters of various sizes. *Dimers* are a type of ion cluster frequently present in ILIS beams which consists of a single ion attached to a neutrally charged cation-anion pair. In the case of a positive ILIS beam, the dimers are composed of two EMI^+ cations and one BF_4^- anion. Another type of ion cluster is the *trimer*, which consist of a single ion attached to two cation-anion pairs. In the case of a positive ILIS beam, the trimers are composed of three cations and two anions. Fig. 1 shows the molecular structure of the positive EMI-BF_4 monomer, dimer, and trimer. Note that monomers and dimers represent the majority of the ion species in ILIS beams, whereas trimers and larger ion clusters are typically present in small fractions [3, 18, 19].

Ion clusters are not stable and will eventually dissociate [5, 8, 9]. Depending on the size of the ion cluster, there can be a variety of dissociation paths [10, 14, 20]. This work concentrates on the case in which a cation-anion pair evaporates from the positively charged parent ion cluster, leaving behind a grouping of ions with a single positive charge. Recent work by Prince et al. suggests that neutral evaporation is a preferred dissociation pathway for ionic liquid ion clusters [13]. For a dimer that dissociates along this path, the evaporation of a cation-anion pair, called a *neutral*, leaves behind a positive monomer. For trimers that dissociate in this way, the evaporation of a neutral leaves behind a positive dimer. Fig. 2 shows the dissociation pathway for a positive EMI-BF_4 dimers. Note that the ion produced by dissociation is called the *broken ion* in this work.

[a]EMI-BF_4 = 1-ethyl-3-methylimidazolium tetrafluoroborate

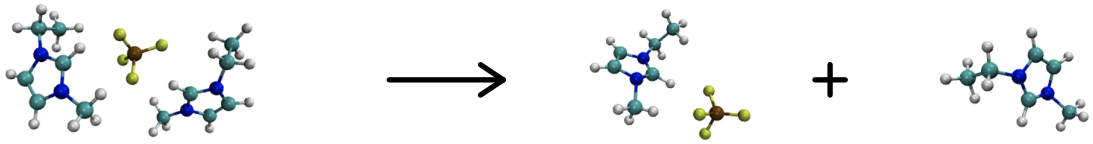

Fig. 2 Positive EMI-BF_4 dimer dissociation through neutral evaporation. [8]

B. Analytical Ion Cluster Dissociation Rate Models

Ion cluster dissociation in ionic liquid ion sources can be modeled as an activated process. The dissociation rate, K, for a particular type of ion cluster, in the absence of an electric field, can be described using an Arrhenius equation: [15]

$$K = A \exp\left[-\frac{E_a}{kT}\right] \tag{1}$$

where A is the rate coefficient, E_a is the activation energy, k is Boltzmann's constant, and T is the ion cluster temperature. The rate coefficient and activation energies for EMI-Im and EMI-FAP were recently measured using differential mobility analysis [15, 21]. Molecular dynamics simulations have also been used to compute the rate coefficients and activation energies for BMI-DCA[b] and EMI-Im[c] [14]. These MD results are supported by collision-induced dissociation measurements of the dissociation rates [14].

The presence of an externally applied electric field lowers the energy barrier for dissociation: [15–17]

$$K = A \exp\left[-\frac{E_a - G(E)}{kT}\right] \tag{2}$$

where $G(E)$ is the energy barrier reduction induced by the electric field. Note that $G(E)$ is a function of the electric field strength, E, and perhaps also depends on the properties of the ionic liquid ions. Note that the natural logarithm of the dissociation rate is a linear function of $G(E)$:

$$\ln K = \ln A - \frac{1}{kT}\left(E_a - G(E)\right) \tag{3}$$

This formulation will be used to compare experimental measurements with various models for $G(E)$.

1. Image Potential Model

An image potential model has been used to describe the electric field-assisted evaporation of ions from the meniscus of an ILIS [16, 17]. The meniscus is modeled as an infinite, planar sheet of perfectly conducting liquid. As an ion evaporates from the liquid bulk, it experiences a force from its image charge, which pulls it back towards the liquid. The evaporating ion also experiences a force from the externally applied electric field, which pulls it away from the liquid, helping it to evaporate. The external electric field reduces the energy barrier for evaporation by an amount given by the following expression: [16]

$$G(E) = \sqrt{\frac{q^3 E}{4\pi\epsilon_0}} \tag{4}$$

where q is the ion charge and ϵ_0 is the permittivity of free space.

The image potential model has also been used to analyze the dissociation of ILIS ion clusters in the acceleration region [9, 10, 12], although its validity in this context requires further study. Consider a dimer ion cluster that dissociates into a monomer and a neutral cluster within the acceleration region. This process can be viewed as the evaporation of a monomer from the dimer cluster in the presence of an electric field. Assuming the neutral behaves as an infinite planar surface of ionic liquid, the electric field will decrease the energy barrier for dissociation by the amount specified by Eq. (4). Here, $G(E)$ is a constant factor, c, multiplied by the square root of the electric field strength: $G(E) = c\,E^{1/2}$. If the IPM accurately captures the physics of ion cluster dissociation in the presence of an external electric field, then the natural logarithm of the dissociation rate of a particular type of ion cluster should vary linearly with the square root of the electric field strength.

[b]BMI-DCA = 1-butyl-3-methylimidazolium dicyanamide
[c]EMI-Im = 1-ethyl-3-methylimidazolium bis(trifluoromethylsulfonyl)imide

2. Dipole Model

The image potential model may not provide the most realistic description of ion cluster dissociation in the presence of an electric field. For example, consider the dissociation of a dimer into a monomer and a neutral. The neutral is composed of two discrete ions, one cation and one anion, so it is unlikely to behave as a planar continuum of ionic liquid. Instead, the neutral is more comparable to an electric dipole. A dipole model has recently been developed by Schroeder to analyze dimer dissociation in the presence of an external electric field [10]. This model has been compared to both the IPM and the results of molecular dynamics simulations [10].

The neutral cluster is modeled as a dipole with separation d, oriented at an angle θ relative to the direction of the external electric field. The evaporating monomer is located at a distance x from the anion within the neutral, measured along the axial direction as shown in Fig. 3(a). The work required to bring the monomer from a sepration distance, x, to infinity is given by $W(x)$: [10]

$$W(x) = \frac{q^2}{4\pi\epsilon_0}\frac{1}{x} - \frac{q^2}{4\pi\epsilon_0}\frac{1}{\sqrt{(x + d\cos\theta)^2 + (d\sin\theta)^2}} + qEx \tag{5}$$

The minimum value of this function, W_{min}, is the amount by which the external electric field reduces the energy barrier for dissociation: $G(E) = W_{min}$ [10]. If the dipole model accurately describes dimer dissociation in the presence of an external electric field, then the natural logarithm of the dimer dissociation rate should vary linearly with W_{min}. Note that the minimum value of $W(x)$ cannot be solved for analytically; however, the value of W_{min} as a function of the electric field strength can be obtained using a numerical approach. Fig. 3(b) shows the energy barrier reduction as a function of the electric field strength for both analytical models. At low electric field strength, the IPM predicts a larger energy barrier reduction compared to the dipole model. However, at field strengths exceeding 10^8 V/m, not shown in Fig. 3(b), the dipole model predicts a larger energy barrier reduction compared to the IPM, for dipole angles greater than 45°.

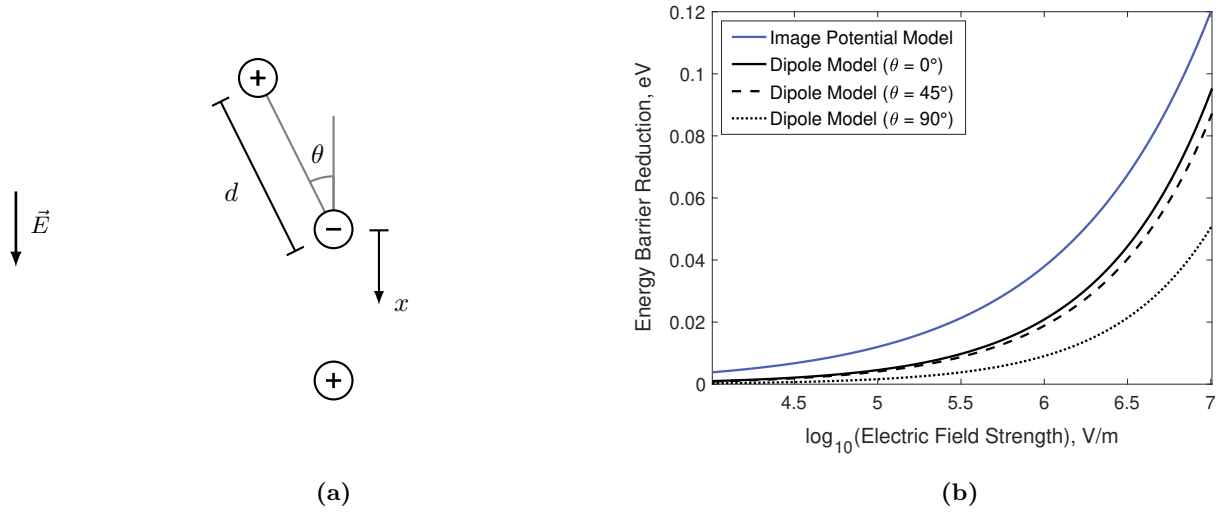

(a) **(b)**

Fig. 3 (a) Schematic of the dipole model adapted from Schroeder [10]. (b) Dimer dissociation energy barrier reduction as a function of electric field strength for both the image potential and dipole models. For the dipole model, the dipole separation is set to 10 Angstroms.

C. Evolution of Ion Cluster Populations in the Acceleration Region

Consider the dissociation of dimers in the acceleration region. Assume that, at a given instant, N_0 dimers are evaporated from the liquid meniscus each with the same temperature, T. After evaporation, the population of dimers evolves, due to dissociation, as they move towards the thruster exit. The percentage of in-tact dimers, meaning dimers that have not dissociated, begins at 100% and steadily decreases as the dimers travel through the acceleration region. The number of dimers that dissociate per unit time is given by the product of the dimer dissociation rate, K, with the

number of in-tact dimers that exist at that instant, N. Thus, the rate of change of the in-tact dimer population within the acceleration region is:

$$\frac{dN}{dt} = -KN \tag{6}$$

Note that t is measured from the instant dimers are evaporated from the meniscus. This formulation assumes that at any instant, all dimers have the same dissociation rate. For this to be true, Eq. 1 suggests that all dimers must have the same temperature. Additionally, the dissociation rate varies with the electric field strength, according to Eq. 2, so all dimers must experience the same electric field at each instant. For this to be true, all dimers must follow equivalent trajectories through the acceleration region.

The electric field strength decreases with increasing distance from the emitter tip. Thus, according to the models outlined in the previous section, the dissociation rate, K, should decrease as dimers move away from the emission site. Additionally, as the dimer population evolves, the number in-tact dimers decreases as a result of dissociation. As a result, the magnitude of the instantaneous rate of change of the dimer population, $\left|\frac{dN}{dt}\right|$, decreases as the dimers approach the exit of the thruster. Outside the ion source, the electric field is zero, which means that the dissociation rate is constant. As a result, the dimer population evolves according to a constant-rate equation in the field-free region, which has been observed in recent RPA measurements [9, 12].

III. Experimental Approach and Design

A. Ion Source

In this work, an externally wetted tungsten needle is used as a single emitter ILIS, which is depicted in Fig. 4. The tungsten needle was electrochemically etched and chemically roughened to produce a tip radius of curvature of approximately 5 micrometers. The needle was coated with EMI-BF_4 ionic liquid and threaded through the center of a cylindrical stainless steel propellant reservoir. The source potential, V_0, is applied to the needle through the distal contact of the reservoir. The extractor plate, with an aperture diameter of 1.6 mm, is held at ground potential (0 V). The ion source was operated at voltages ranging from 1720 V to 2020 V. An Arduino PID controller was used in conjunction with a heater and thermocouple to maintain a constant ionic liquid temperature [22]. The ion source was operated at temperatures ranging from 30°C to 110°C.

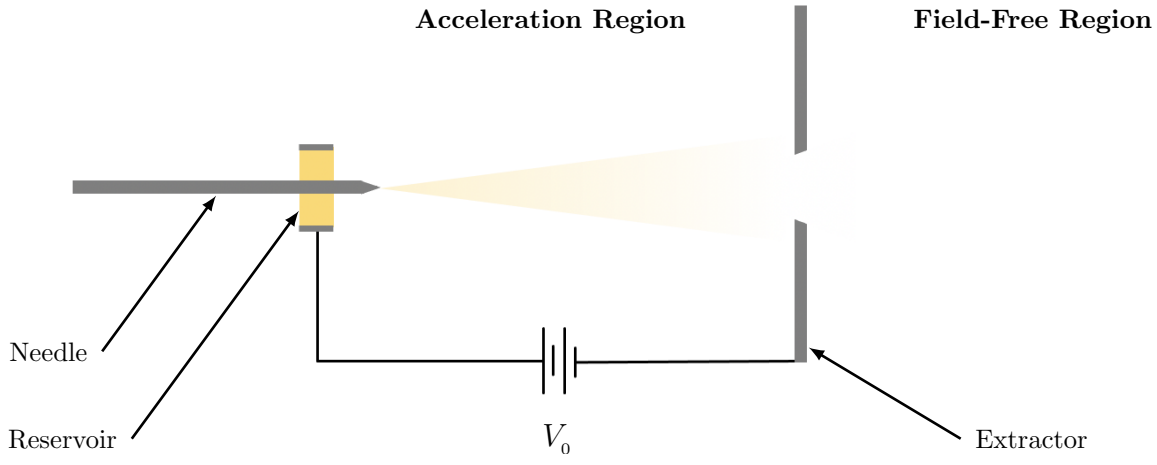

Fig. 4 Tungsten needle single emitter ILIS.

B. Time of Flight Mass Spectrometry

Time of flight (TOF) mass spectrometry can be used to determine the relative fractions of monomers, dimers, trimers, and other heavy ion cluster species in an ILIS beam. It can also be used to measure the amount of dissociation within the acceleration region for specific ion cluster species. With sufficient resolution, TOF measurements can be used to estimate the acceleration region dissociation rates of particular ion cluster species. The TOF instrumentation used in this work, shown in Fig. 5, consists of an electrostatic deflection gate and a Channeltron electron multiplier collector [22]. The gate and collector are separated by a flight length of $L = 0.77$ m. The collector signal is amplified by a non-inverting amplifier circuit, the design of which is detailed in the Appendix, and then measured by an oscilloscope.

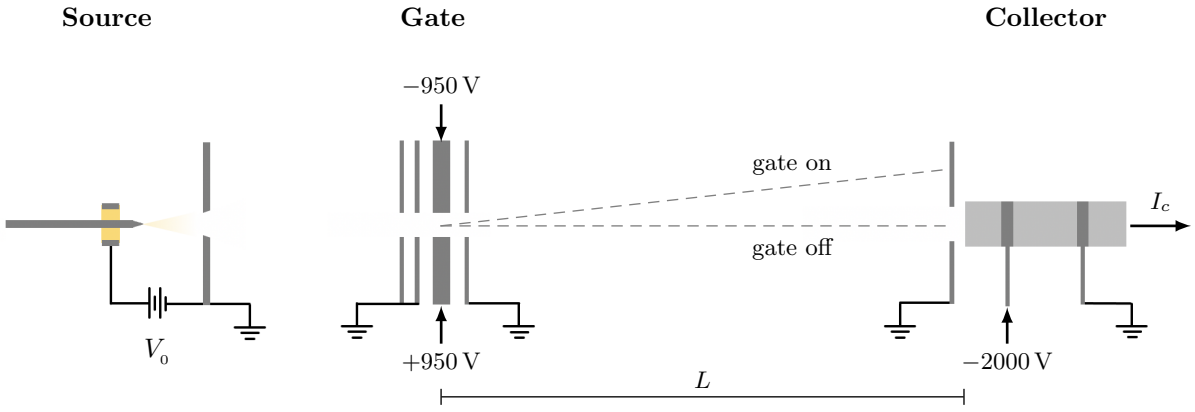

Fig. 5 Schematic of the time of flight instrumentation.

A TOF measurement consists of the collected current as a function of time. The flight time, t_f, of an ion with constant speed, v, that travels through a flight length, L, is given by: $t_f = L/v$. Since there are no axial electric fields outside of the source, the speed of an ion remains constant as it travels towards the TOF detector. Thus, the speed at which an ion travels between the gate and collector is the speed at which it leaves the source. Consider an ion that does not dissociate in the acceleration region. In this work, these ions are referred to as *monoenergetic* since their mechanical energy is $q\phi_0$, which is the maximum possible energy the ions can have. Note that ϕ_0 is the electric potential difference through which the ion is accelerated. Typically, ϕ_0 is ~ 98% of the potential applied to the source, V_0 [5]. The exit speed, v_i, of a monoenergetic ion of mass m_i is given by:

$$v_i = \sqrt{\frac{2q\phi_0}{m_i}} \tag{7}$$

The lightest ions leave the source with the highest speeds; thus, they have the shortest flight times. All monoenergetic ions with the same mass arrive at the TOF detector at the same time. As a result, the TOF curve is composed of vertical steps, one for each type of monoenergetic ion species. For example, Fig. 6(a) shows a normalized, idealized TOF curve for an ILIS beam that consists of 50% monoenergetic monomers and 50% monoenergetic dimers. For a normalized TOF curve, the height of a particular step corresponds to the beam fraction for that particular ion species.

Now consider a broken ion, of mass m_{bi}, produced by the dissociation of a parent ion cluster, of mass m_{pi}, in the acceleration region. The exit speed, v_{bi}, of the broken ion is given by:

$$v_{bi} = \sqrt{{v_0}^2 + \frac{2q}{m_{pi}}\left(\phi_0 - \phi_{br}\right) + \frac{2q}{m_{bi}}\phi_{br}} \tag{8}$$

where ϕ_{br} is the value of the electric potential at the location where the dissociation event occurred. This equation is derived in the Appendix. In formulating this expression, it was assumed that the broken ion is produced from a single dissociation event within the acceleration region. For example, a dimer that evaporates from the liquid meniscus and later dissociates into a monomer and a neutral pair is considered a single dissociation event. Eq. 8 does not apply to the case in which a trimer is evaporated from the liquid meniscus and later dissociates into a dimer that later dissociates into a monomer, with both events occurring within the acceleration region.

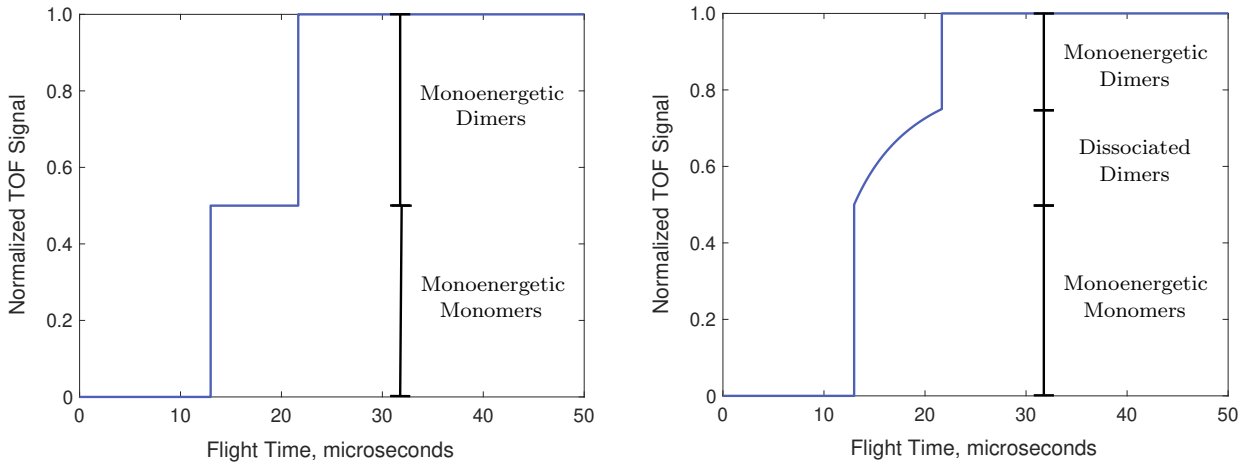

Fig. 6 Normalized, idealized TOF curves for a positive EMI-BF_4 ILIS beam: (a) without fragmentation, (b) with dimer fragmentation. The source potential is V_0 = 2020 V and the flight distance is L = 0.77 m.

The final speed of a broken ion depends on the electric potential at the break-up location, ϕ_{br}. Consider the case in which the parent ion is a dimer. If the dimer dissociates close to the liquid meniscus where $\phi_{br} \approx \phi_0$, then the broken ion, a monomer, exits the source with approximately the same speed as monoenergetic monomers. If the dimer dissociates close to the extractor plate where $\phi_{br} \approx 0$, then the broken ion exits the source with approximately the same speed as monoenergetic dimers. If the dimer breaks up somewhere in between the meniscus and extractor plate, then the broken ion exits the source with a speed in between that of a monoenergetic monomer and a monoenergetic dimer. As a result, the flight times of broken ions produced by dimer dissociation within the acceleration region range from that of a monoenergetic monomer to that of a monoenergetic dimer.

Fig. 6(b) shows a normalized, idealized TOF curve for an ILIS beam that consists of 50% monoenergetic monomers, 25% monoenergetic dimers, and 25% dimers that dissociate in the acceleration region. In other words, 50% of the ions evaporated from the meniscus are dimers; however, only 50% of those dimers exit the source intact. Note that, in generating the idealized TOF curve in Fig. 6(b), it was assumed that the amount of dimer dissociation is uniform with respect to electric potential. Prior experimental work has demonstrated that the amount of dissociation varies linearly with electric potential in the low-field section of the acceleration region [8, 9, 12]. This assumption may not apply in the high-field region close to the emission site.

A TOF curve provides a voltage signal which is a function of the flight time, $s(t_f)$, which is proportional to the collected ion current, given sufficient amplifier bandwidth (see Appendix). Thus, the TOF curve provides the amount of dissociation of a particular type of ion species as a function of the flight time: $s_{bi}(t_f)$. Given the flight distance, L, and the flight time of a broken ion, t_f, the value of the electric potential where the parent ion broke up, ϕ_{br}, is:

$$\phi_{br} = \frac{\frac{m_{bi}}{2q}\left(\left(\frac{L}{t_f}\right)^2 - {v_0}^2\right) - \frac{m_{bi}}{m_{pi}}\phi_0}{1 - \frac{m_{bi}}{m_{pi}}} \tag{9}$$

The amount of dissociation as a function of the electric potential, $s_{bi}(\phi_{br})$, can be determined using this mapping.

The amount of dissociation with respect to time spent in the acceleration region, for a particular type of parent ion, is needed to obtain the acceleration region dissociation rates for that type of parent ion. Note that the flight time, t_f, and the time a parent ion spends in the acceleration region before breaking up, t, are different quantities. An ion trajectory model is necessary to determine the time it takes a parent ion to travel from the emission site to a particular location within the acceleration region. Such a model would provide a mapping between the electric potential at the location where the parent ion dissociates and the time it takes the parent ion to reach that location. The amount of dissociation with respect to electric potential, $s_{bi}(\phi_{br})$, can then be converted to the amount of dissociation with respect to time spent in the acceleration region: $s_{bi}(t)$. Given this distribution, Eq. 6 can be used to extract the dissociation rates for a particular parent ion species throughout the acceleration region.

C. Acceleration Region Trajectory Model

1. Laplacian Electric Field Model

A two-dimensional, cylindrically symmetric geometry of the needle tip and extractor was created using MATLAB. The emitter tip edge is described using prolate spheroidal coordinates [23] with a tip radius of curvature of 5 micrometers and extractor distance of 250 micrometers. The extractor thickness is 0.64 mm and the extractor aperture diameter is 1.6 mm. The electric potential distribution within the acceleration region was obtained by numerically solving Laplace's equation: $\nabla^2\phi = 0$. The geometry edge corresponding to the surface of the needle was given a Dirichlet boundary condition of $\phi = \phi_0$. The geometry edges corresponding to the surface of the extractor were given a Dirichlet boundary condition of $\phi = 0$. All other edges were given a Neumann boundary condition of zero flux through the edge. Fig. 7(a) shows a colormap of the electric potential distribution within the acceleration region.

The electric field distribution was determined using numerical differentiation, since $\vec{E} = -\nabla\phi$. Of greatest interest is the electric field along the axial direction, $E(z)$. Note that the z-axis points from the center of the emitter tip through the center of the extractor aperture. Fig. 7(b) shows the axial electric field strength as a function of the distance from the emitter tip, z. Note that the Laplacian model does not capture the enhancement of the electric field due to the sharpened liquid meniscus. Including this effect is not strictly required to estimate the dissociation rates several emitter radii away from the emission site. However, to determine the dissociation rates close to the meniscus, accurately modeling this effect is essential.

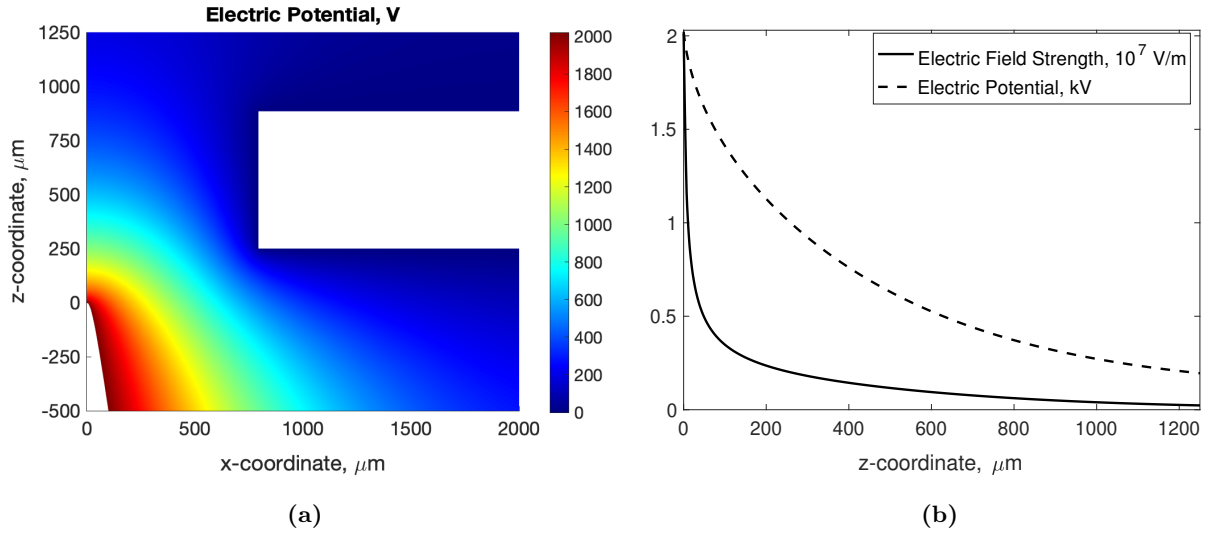

Fig. 7 (a) Electric potential distribution within the acceleration region. (b) Electric potential and axial electric field strength along the ion flight path. The source potential was set to V_0 = 2020 V.

2. Ion Trajectory Integration

Under the assumption that ions are evaporated from the center of the emitter and are accelerated in the axial direction by the electric field, ion trajectory analysis becomes a one-dimensional problem. The equation of motion for a parent ion in the acceleration region is:

$$qE(z) = m_{pi}\frac{d^2z}{dt^2} \tag{10}$$

Note that electrostatic forces from nearby ions in the beam are neglected in this analysis. Given the electric field model detailed in the previous subsection, the trajectory of the parent ion can be determined using numerical integration. Fig. 8(a) shows the trajectories of positive EMI-BF_4 dimers and trimers. Fig. 8(b) shows the mapping between the electric potential and the time a parent ion spends in the acceleration region.

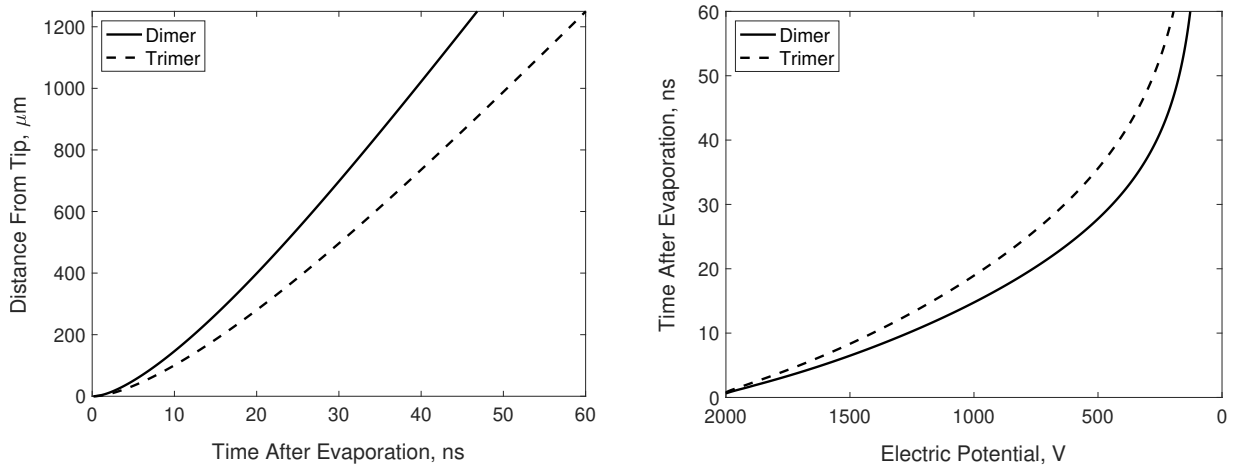

(a) (b)

Fig. 8 (a) Positive EMI-BF_4 ion cluster trajectories along the axial direction. (b) Mapping between electric potential and time spent in the acceleration region for positive EMI-BF_4 ion clusters. The source potential is V_0 = 2020 V and the initial ion speed is v_0 = 0 m/s.

IV. Data Analysis

This section outlines the various steps of the analysis process, which include normalization, step height determination, fitting of dissociated ion signal, computation of the intact parent ion fraction, and computation of the dissociation rates.

1. Normalization

Each TOF curve was normalized by first subtracting the baseline signal level and then dividing by the total signal amplitude. The baseline signal is set to the average signal between 5 μs and 10 μs. The maximum signal is set to the average signal between 45 μs and 50 μs. The total signal amplitude is the maximum signal minus the baseline signal. Fig. 9(a) shows normalized TOF curves for a source potential of 2020 V at various ionic liquid temperatures.

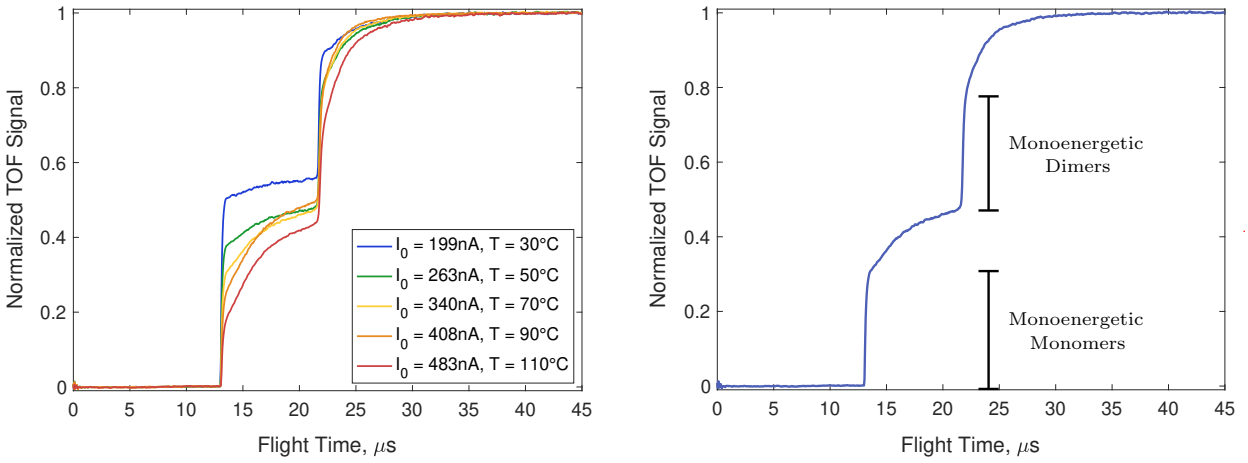

(a) (b)

Fig. 9 (a) Normalized TOF curves for V_0 = 2020 V at various ionic liquid temperatures. (b) Normalized TOF curve for V_0 = 2020 V, T = 70°C with monoenergetic monomer and dimer steps labeled.

2. Step Height Determination

The step heights for monoenergetic monomers, dimers, and trimers were determined for each TOF curve. This process was completed manually through the selection of points on the TOF data graph. The base of a step is the point where the TOF signal begins to rapidly increase. The top of a step is the point where the step levels off, usually right before the measurement noise reappears. Note that the step signal is smooth because the TOF amplifier has limited bandwidth. The measurement noise reappears in the signal after the amplifier slews to the voltage level that corresponds to the top of the step. Fig. 9(b) shows the monoenergetic monomer and monoenergetic dimer step heights for a source potential of 2020 V at an ionic liquid temperature of 70°C.

3. Dissociated Ion Signal Fitting

The signal corresponding to dimers that dissociate in the acceleration region lies between the end of the monoenergetic monomer step and the beginning of the monoenergetic dimer step. The signal corresponding to trimers that dissociate in the acceleration region lies between the end of the monoenergetic dimer step and the beginning of the monoenergetic trimer step. The data corresponding to each type of dissociated parent ion are extracted from the TOF curve for further processing. The extracted data for a particular type of dissociated parent ion are binned in order to reduce noise. The bin width was set to 0.25 μs.

A selection window with lower and upper bounds on the flight time is used to isolate dissociated parent ion data for fitting. The lower bound is defined as the flight time for which a parent ion breaks at $\phi_{br} = 0.8\phi_0$. This cutoff value was selected in order to avoid using data that may be distorted by the delayed amplifier response (see the Appendix for further discussion). The upper bound is defined as the flight time for which a parent ion breaks at $\phi_{br} = 0.1\phi_0$. This cutoff value was selected in order to avoid using data that may be distorted by the arrival signal of the monoenergetic parent ions. Additionally, the electric field model is not reliable for $\phi < 0.1\phi_0$ due to boundary effects on the PDE solution.

The binned data points that lie within the selection window are fitted using a spline curve with the following constraints: positive first derivative, negative second derivative, and positive third derivative. These constraints require the fitted curve to reflect that the amount of dissociated parent ions steadily increases at a rate which decreases as the intact parent ions move through the acceleration region. Fig. 10(a) shows the dissociated dimer fitted data for a source potential of 2020 V at an ionic liquid temperature of 70°C.

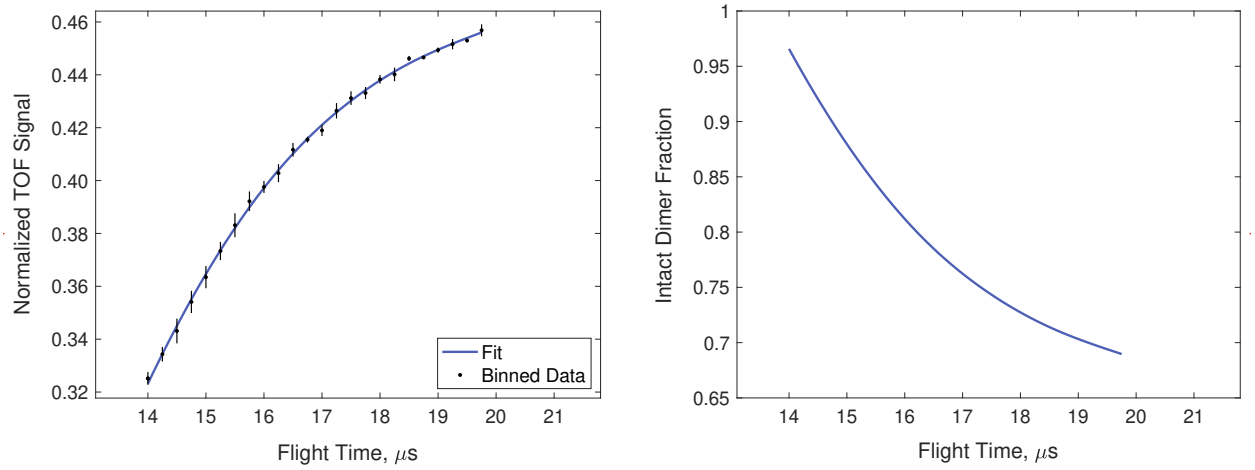

(a) (b)

Fig. 10 (a) Fit of dissociated dimer signal and (b) intact dimer fraction for V_0 = 2020 V, T = 70°C. These quantities are plotted as a function of flight time. The lower bound on the horizontal axis is 13.1 μs, which is the flight time of a monoenergetic monomer for these particular source parameters. The upper bound on the horizontal axis is 21.8 μs, which is the flight time of a monoenergetic dimer for these particular source parameters. Note that the fit is only applied to the dissociated dimer data with flight times that correspond to $0.1\phi_0 < \phi_{br} < 0.8\phi_0$.

4. Intact Parent Ion Fraction Computation

The dissociated ion signal, $s_{bi}(t_f)$, is used to compute the fraction of intact parent ions as a function of flight time: $f_{pi}(t_f)$. The fraction of intact parent ions begins at 100% and steadily decreases as the dissociated ion population increases. The following expression is used to compute the fraction of intact parent ions as a function of the flight time of the broken ions, $f_{pi}(t_f)$:

$$f_{pi}(t_f) = 1 - \frac{s_{bi}(t_f)}{s_{pi}} \tag{11}$$

where s_{pi} is the total beam fraction of parent ions, including those that dissociate. The total beam fraction of parent ions, both intact and dissociated, is readily determined using the monoenergetic step boundaries. For example, the beam fraction of dimers is given by the signal at the top of the monoenergetic dimer step minus the signal at the top of the monoenergetic monomer step. Similarly, the total beam fraction of trimers is given by the signal at the top of the monoenergetic trimer step minus the signal at the top of the monoenergetic dimer step. Note that the TOF signal must be normalized to compute the ion fractions in this way. As an example, the fraction of intact dimers as a function of flight time for a source potential of 2020 V at an ionic liquid temperature of 70°C is shown in Fig. 10(b).

5. Dissocation Rates Computation

In order to determine the dissociation rates for a particular type of parent ion, the fraction of intact parent ions as a function of time after evaporation is needed. The fraction of intact parent ions as a function of flight time, $f_{pi}(t_f)$, was determined in the previous data analysis step. Using Eq. 9, the flight time can be mapped to the break-up potential, ϕ_{br}, which yields: $f_{pi}(\phi_{br})$. Next, using the ion trajectory model, the break-up potential can be mapped to the time after evaporation, t, which yields: $f_{pi}(t)$. The fraction of intact dimers as a function of time after evaporation for a source potential of 2020 V at an ionic liquid temperature of 70°C is shown in Fig. 11(a).

The time rate of change of the intact parent ion fraction, $\frac{f_{pi}(t)}{dt}$, is also needed to determine the dissociation rates. The intact parent ion fraction as a function of time after evaporation, $f_{pi}(t)$, is fitted using a spline and is numerically differentiated to obtain $\frac{f_{pi}(t)}{dt}$. The time rate of change of the intact dimer fraction for a source potential of 2020 V at an ionic liquid temperature of 70°C is shown in Fig. 11(b). The parent ion dissociation rate as a function of time after evaporation is found using a normalized version of Eq. 6:

$$\frac{df_{pi}(t)}{dt} = -K f_{pi}(t) \tag{12}$$

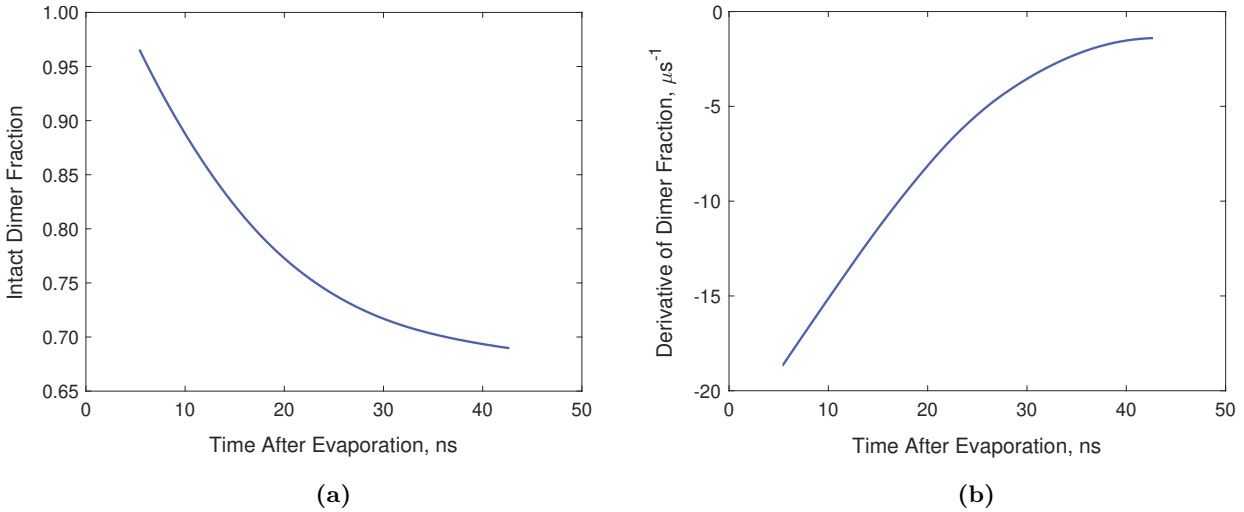

Fig. 11 (a) Intact dimer fraction and (b) time derivative of the intact dimer fraction as a function of time after evaporation for V_0 = 2020 V, T = 70°C.

The dissociation rate as a function of the electric field strength can be determined by mapping the time after evaporation back to the break-up potential. Using the Laplacian field model, the break-up potential can be mapped to the electric field strength, E. Fig. 12 shows the dimer dissociation rate and mean lifetime as functions of the electric field strength within the acceleration region for a source potential of 2020 V at an ionic liquid temperature of 70°C. Note that the mean lifetime of the parent ions is the inverse of the dissociation rate: $\tau = 1/K$.

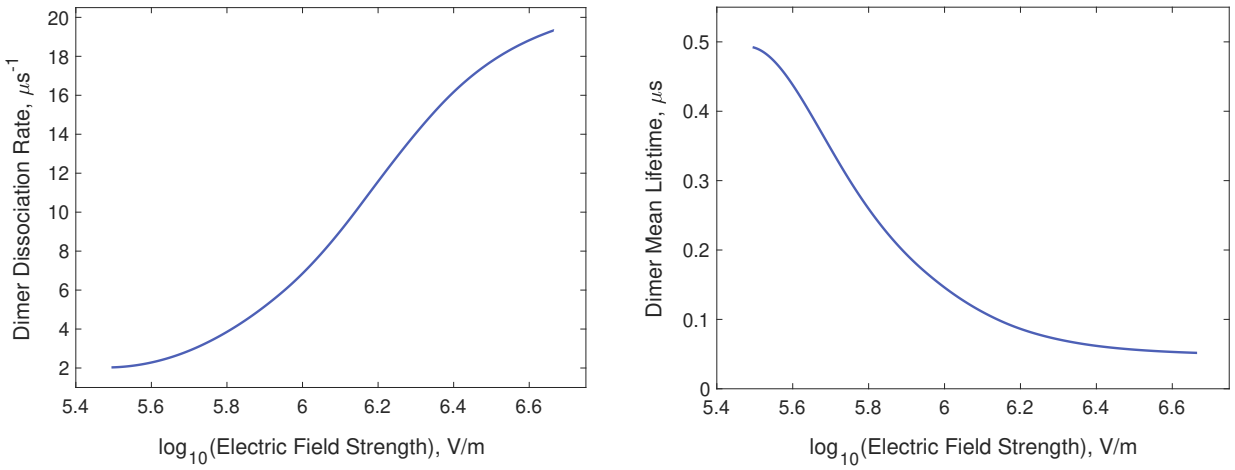

(a) (b)

Fig. 12 (a) Mean dimer dissociation rate and (b) dimer mean lifetime as functions of the acceleration region electric field strength for V_0 = 2020 V, T = 70°C.

V. Results

A. Dimer Dissociation in the Acceleration Region

Fig. 13 shows the dimer mean lifetime as a function of acceleration region electric field strength for various source potentials and ionic liquid temperatures. Note that these plots are on a logarithmic scale.

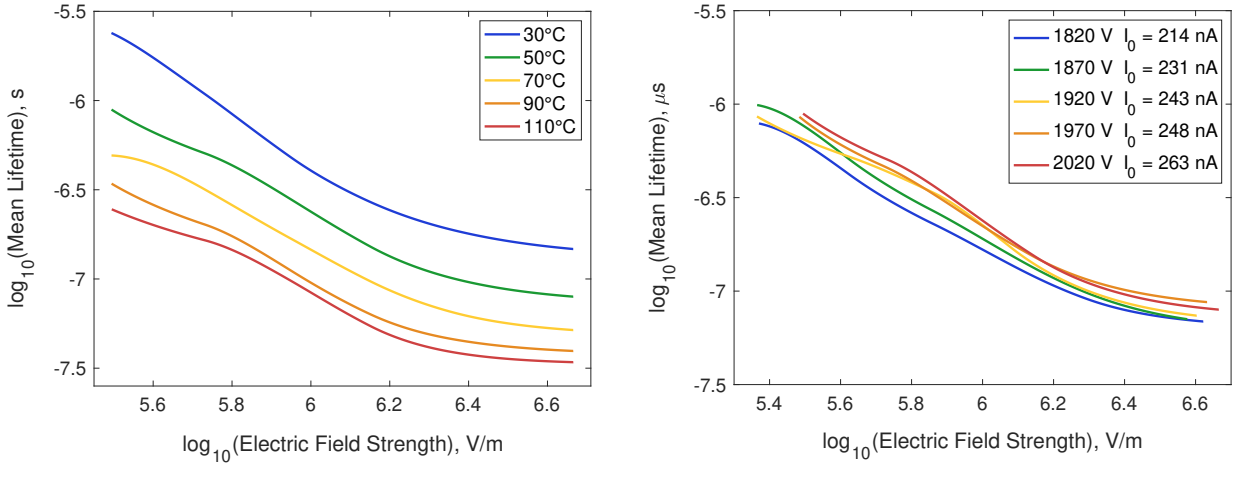

(a) (b)

Fig. 13 Dimer mean lifetime as a function of the electric field strength for (a) V_0 = 2020 V at various temperatures and (b) T = 50°C at several source voltages. The source currents for (a) are listed in Fig. 9(a).

Fig. 14 shows the intact dimer fraction and mean dimer dissociation rates as a function of the normalized electric potential within the acceleration region for $T = 50°C$ at various source voltages.

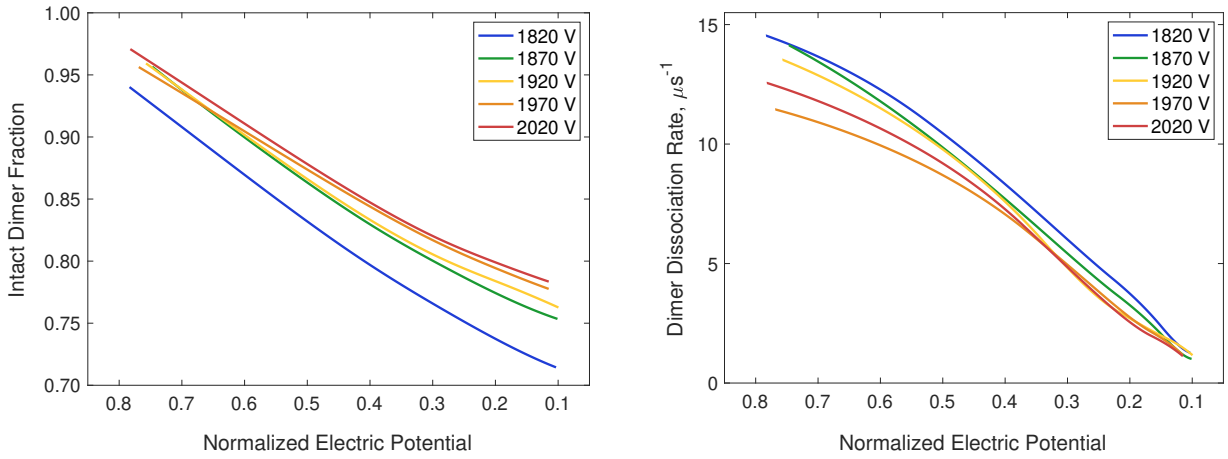

(a) (b)

Fig. 14 (a) Intact dimer fraction and (b) Dimer dissociation rate for T = 50°C at various source voltages. These quantities are plotted as functions of the normalized acceleration region electric potential (ϕ/ϕ_0).

Note that the dissociation rates for trimers are not reported since the trimer results were not as robust as those for the dimers. As such, trimer dissociation requires further analysis as future work.

B. Comparison with Analytical Models

Eq. 3 is used to compare the experimentally measured mean dissociation rates with the image potential model and dipole models. Fig. 15(a) shows the natural logarithm of the dimer dissociation rate as a function of the square root of the electric field strength. Fig. 15(b) shows the natural logarithm of the dimer dissociation rate as a function of the dipole model minimum work for various dipole angles. Note that the dipole separation was set to 10 Angstroms.

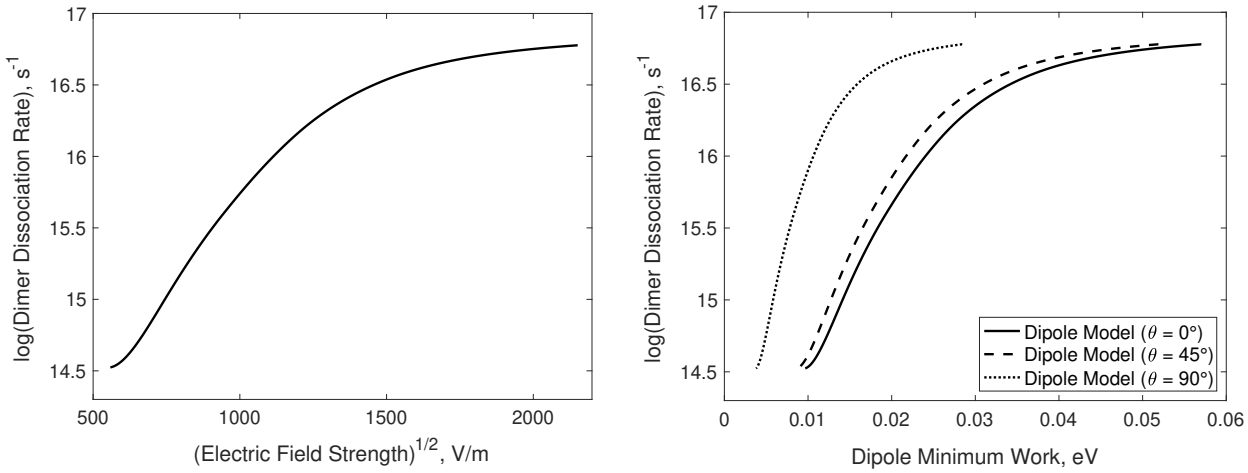

(a) (b)

Fig. 15 Comparison of experimentally measured mean dimer dissociation rates in the acceleration region for V_0 = 2020 V at T = 70°C with (a) the image potential model and (b) the dipole model.

VI. Discussion

It is critical to note that each data point in Fig. 13 represents an average lifetime of the entire intact dimer population at a given instant in time. If all of the intact dimers have the same temperature and experience the same electric field strength at a given instant in time, then the measured average lifetime for the intact dimer population as a whole is the same as the lifetime for an individual dimer at that particular temperature and electric field strength. Realistically, the intact dimers will have a distribution of temperatures [8, 10]. Additionally, the intact dimers will follow different paths through the acceleration region, and thus may experience different electric field strengths at different times. Thus, the measured lifetimes in Fig. 13 should only be interpreted as average quantities for the dimer population as a whole.

Setting aside the effect of an external electric field, consider the effect of a temperature distribution with non-negligible width. Assume the intact dimer population has an initial temperature distribution, $f_{di}(T)$. Perhaps this temperature distribution can be modeled as a Gaussian function centered on an initial mean temperature, T_0. According to Eq. 1, the dimers with higher temperatures have higher dissociation rates than the dimers with lower temperatures. As the dimer population evolves over time, the high-temperature dimers dissociate faster than the low-temperature dimers. As a result, the temperature distribution of the intact dimers shifts towards lower temperatures. Thus the mean temperature at any given time, $\overline{T}(t)$, will be less than the initial mean temperature, T_0. By Eq. 1, the average lifetime of the intact dimer population, as a whole, increases over time as a result of the shifting temperature distribution. The magnitude of this effect depends on the initial width of the temperature distribution and thus the initial spread in individual dimer lifetimes. Such quantities could be estimated using molecular dynamics simulations and would be beneficial for interpreting the experimental measurements reported in this work.

Now consider the effect of an external electric field on the dimer population. The acceleration region electric field strength is maximum at the emission site and decays rapidly towards the thruster exit. According to Eq. 2, the high field strength near the emission site enhances the dissociation rates. As the dimers move away from the meniscus, the electric field strength decreases, thus the mean dissociation rate should also decrease. If the dimers experience the same electric field strength at any given instant in time, then the effect of the electric field should be uniform across the dimer population. Realistically, the dimers will travel along different trajectories in the acceleration region, so it is expected that, at any given moment, some dimers will experience different field strengths than others. Additionally, depending on the paths taken, dimers that evaporate at the same time may exit the source at different times. Fortunately, the TOF instrumentation used in this work has a narrow acceptance angle. This should guarantee that any dimers collected by the detector travel along an axial trajectory through the acceleration region.

Fig. 13 shows that the dimer population mean lifetime increases as the electric field strength decreases for a given set of source parameters. The mean lifetime increases by an order of magnitude as the electric field strength decreases by an order of magnitude. However, without the values of the rate constant and activation energy for positive EMI-BF_4 dimers, it is difficult to deconvolve the effects of the external electric field and the shifting dimer temperature distribution. The lowest electric field strength corresponds to the location where $\phi_{br} = 0.1\phi_0$, which is close to the exit of the thruster. For an ionic liquid temperature of 50°C, the mean lifetime at this point is ~ 1 μs, as shown by Fig. 13(b). According to previous work [9], this value is on the order of magnitude expected for positive EMI-BF_4 dimers at the source exit. More direct comparisons with previous work cannot be made due to the differences in source design, which results in significant differences in source potential and current.

For a given source potential, the mean lifetime varies significantly with ionic liquid temperature, as shown in Fig. 13(a). The shape and amplitude of each curve is approximately the same for each ionic liquid temperature. This indicates that effect of the electric field is relatively independent from the effect of ionic liquid temperature. The curve for the lowest ionic liquid temperature, 30° C, has the longest mean lifetimes. As the ionic liquid temperature increases, the curves shift towards shorter lifetimes. The mean lifetimes for an ionic liquid temperature of 30°C are nearly an order of magnitude larger than those for 110°C. By Eq. 1, a higher dimer temperature results in a higher dissociation rate, and thus a shorter mean lifetime. Thus, heating the ionic liquid increases the mean dimer temperature. Note that the change in ionic liquid temperature is not necessarily equal to the change in mean dimer temperature.

The variation in ionic liquid temperature also corresponds to a significant variation in source current. As the ionic liquid temperature is increased from 30°C to 110°C (a factor of 3.7), the source current increases from 199 nA to 483 nA (a factor of 2.4). Increased source current leads to increased Ohmic heating of the emission site [24, 25], which raises the local ionic liquid temperature. The mean dimer temperature upon evaporation should increase as a result of the increased source current, which would decrease the initial mean lifetime of the dimer population. Additionally, increased source current is associated with changes to the beam composition, as shown in Fig. 9. As the ionic liquid temperature and source current increase, the fraction of monoenergetic monomers decreases, the total fraction of dimers increases,

and the dissociated dimer fraction increases. These observations suggest that the characteristics of the emission site changes with source current, which could affect the temperature distribution of the evaporated ion clusters in ways beyond the direct effects of Ohmic heating.

For a given ionic liquid temperature, the mean lifetime varies only slightly with source potential, as shown in Fig. 13(b). The source potential ranges from 1820 – 2020 V, which corresponds to source currents of 214 – 262 nA. As the source potential increases from 1820 V to 2020 V (by 10%), the source current increases from 214 nA to 262 nA (by 22%). As the source potential is increased from 1820 V to 2020 V, the mean lifetimes decrease by ~ 50%. This trend is somewhat unexpected since increasing the source potential also increases the source current, which, based on the data shown in Fig. 13(a), is associated with decreased mean lifetime. Increasing the source potential increases the electric field strength in the acceleration region, which should enhance the dissociation rates near the emission site. In terms of the beam composition, as measured by the TOF instrumentation, increasing the source potential results in an increasing monomer fraction, an increasing total dimer fraction, and a decreasing dissociated dimer fraction.

Fig. 14(a) shows the intact dimer fraction as a function of the normalized electric potential within the acceleration region for $T = 50°C$ at various source voltages. For $0.35 < \phi/\phi_0 < 0.75$, the amount of intact dimers decreases linearly with electric potential. This relationship is also observed in RPA measurements where the slopes corresponding to dissociation in the acceleration region are approximately linear with respect to electric potential [6, 8, 9, 12]. Fig. 14(b) shows the dimer dissociation rate as a function of the normalized electric potential within the acceleration region for $T = 50°C$ at various source voltages. Between $0.35 < \phi/\phi_0 < 0.75$, the mean dissociation rate decreases by approximately a factor of 2. This modest change in dissociation rate helps explain why the amount of dimer dissociation is approximately linear with electric potential throughout much of the low-field section of the acceleration region.

The experimentally measured mean dimer dissociation rates are compared with the image potential and dipole models in Fig. 15. Fig. 15(a) shows the comparison of experimental measurements with the image potential model. According to Eq. 3 and Eq. 4, the natural logarithm of the dimer dissociation rate should vary linearly with the square root of the electric field strength. The relationship in Fig. 15(a) is not linear, which indicates that the IPM is not a good description for ion cluster dissociation in the presence of an external electric field. However, considering that the measured dissociation rates are a function of the evolving temperature distribution of the dimer population, Fig. 15(a) may not represent a fair comparison. If it were possible to measure the acceleration region dissociation rates for a fixed dimer temperature, then Eq. 3 and Eq. 4 could be used to better test the validity of the IPM in this context.

Fig. 15(b) shows the comparison of experimental measurements with the dipole model [10]. According to Eq. 3, the natural logarithm of the dimer dissociation rate should vary linearly with the minimum work required to evaporate a monomer. The relationship in Fig. 15(b) is not linear for any of the dipole angles tested, which suggests that the dipole model with a fixed dipole angle may not be a good description for ion cluster dissociation in the presence of an external electric field. The dipole model averaged over a range of dipole angles may provide different results. Considering that the measured dissociation rates are averaged over the dimer population, which has a shifting temperature distribution, Fig. 15(b) may not represent a fair comparison. As in the case with the image potential model, if it were possible to measure the acceleration region dissociation rates for a fixed dimer temperature, then Eq. 3 and Eq. 5 could be used to better evaluate the dipole model.

Finally, the measured dimer dissociation rates can be compared to recent molecular dynamics simulations [10]. Schroeder determined the mean lifetimes of positive EMI-BF_4 dimers at various ion temperatures and external electric field strengths. For the electric field strengths probed in this work, 3×10^5 V/m – 5×10^6 V/m, the MD mean lifetimes for dimer temperatures ranging from 1000 – 3000 K are several orders of magnitude shorter than the experimentally measured mean lifetimes. According to the MD results, the mean lifetime for a dimer with a temperature of 1000 K at a field strength of 4×10^5 V/m is ~ 15 ns. This is approximately one hundred times faster than the experimentally measured lifetime for the same electric field strength. Considering that the mean lifetime increases with decreasing ion temperature, this suggests that the mean dimer temperature is well below 1000 K. Molecular dynamics data were not available at lower ion temperatures for the electric field strengths considered in this work.

VII. Conclusion

In this work, time of flight mass spectrometry was used to experimentally determine the dissociation rates of positive EMI-BF_4 dimers within the acceleration region of a single emitter ionic liquid ion source. The source was operated at a range of source potentials (1720V −2020V) and ionic liquid temperatures (30°C – 110°C). It was observed that the dimer mean lifetimes decrease significantly with increasing ionic liquid temperature and source current. The dimer mean lifetimes remained relatively constant with changes to the source potential. The dimer mean dissociation rates

were determined as a function of the acceleration region electric field strength, which provided the opportunity for comparison with analytical and numerical models. Neither the image potential or dipole model predictions were in agreement with the experimentally measured trends. However, the experimentally measured dimer dissociation rates are a function of the mean dimer temperature, which shifts towards lower temperatures as the dimer population evolves. If it were possible to measure the dimer dissociation rates for a fixed dimer temperature, then a fairer comparison could be made with model predictions. The experimentally measured dimer mean lifetimes were compared to recent molecular dynamics results [10]; however, in order to make a direct comparison, molecular dynamics simulations of positive, low-temperature EMI-BF_4 dimers in the presence of low electric field strengths are needed.

Future work includes making improvements to the TOF instrumentation, which are detailed in the Appendix. With increased amplifier bandwidth and decreased bandwidth requirements, it should be possible to determine the dissociation rates at higher electric field strengths. This would provide the dissociation rates close to the emission site, which could be compared to existing molecular dynamics results. Note that the electric field model would need to include the effects of the sharpened meniscus geometry when analyzing the dissociation rates near the emission site. Another strategy to probe the dissociation rates near the meniscus would be to develop a model of the TOF amplifier electronics. Such a model would take the measured amplifier output signal and convert it to the amplifier input signal. Note that that the amplifier output signal is distorted by the bandwidth limitations of the amplifier, whereas the input signal is not (see Appendix for further discussion). Once the input signal is isolated, the data analysis process detailed in this work could be used to determine the dissociation rates near the emission site.

Molecular dynamics could also be used to simulate expected TOF measurements for a given set of source parameters. First, MD could be used to estimate the temperature distribution of the dimer population upon evaporation. Next, MD could be used to determine the dissociation rates as a function of the electric field strength for a particular dimer temperature. This should be done for a range of dimer temperatures that correspond to those of the initial temperature distribution. Then, the evolution of the dimer population through the acceleration region could be simulated, perhaps using methods similar to those described in recent work by Petro et al. [26]. These simulations would provide the intact dimer fraction as a function of time after evaporation. Next, using the method outlined in this work, the mean dissociation rate for the dimer population as a whole can be determined as a function of the electric field strength. The intact dimer fraction and mean dissociation rate of the dimer population are both quantities that can be directly compared to TOF measurements. The TOF measurements and MD simulations could be used together in order to constrain the dimer dissociation rates in the presence of an external electric field for a fixed dimer temperature.

Appendix

A. Time of Flight Amplifier Design and Analysis

Fig. 16 shows a circuit diagram of the non-inverting amplifier with gain used to amplify the output signal of the TOF collector. This circuit was designed to maximize both gain and bandwidth. The 1000 Ω shunt resistor and the AD8067 amplifier provide a combined gain of $G = 10^5$. The AD8067 amplifier is set to a gain of 100, which results in a bandwidth of $BW = 3$ MHz [27]. The 10% to 90% step response rise time, t_r, can be approximated by: [28]

$$t_r = \frac{0.35}{BW} \tag{13}$$

A bandwidth of 3 MHz results in a 117 ns rise time. Not shown in the diagram is the approximately 50 pF capacitance between the amplifier positive input and ground. This capacitance, along with the shunt resistor, form an RC circuit, which introduces additional bandwidth limitations. The bandwidth of an RC circuit is:

$$BW = \frac{1}{2\pi RC} \tag{14}$$

where R is the resistance and C is the capacitance [28]. The 1000 Ω shunt resistance and 50 pF capacitance results in a 3.2 MHz bandwidth, which corresponds to a rise time of 110 ns. The AD8067 response and RC circuit response combine non-linearly to produce the net response of the amplifier.

Consider the amplifier response to the monoenergetic monomer signal. Assume all of the monoenergetic monomers impact the CEM detector at time t_0. The monoenergetic monomer signal, as collected by the CEM, is a vertical step increase in current. However, due to its limited bandwidth, the amplifier produces a rounded step signal. Fig. 17(a) shows the experimentally measured amplifier response to the monomer step and a SPICE model response to a step input

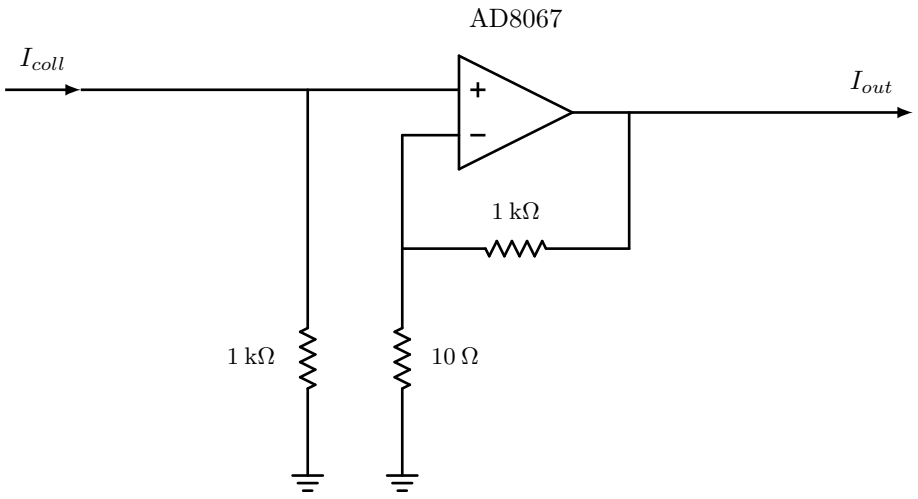

Fig. 16 Schematic of TOF amplifier circuit.

signal of the same amplitude. The 10% to 90% rise time of the model signal is 190 ns, which is in agreement with the analytical analysis above. The rise time of the experimentally measured signal is 296 ns, which is significantly longer than that of the model. Given this discrepancy, the experimental input signal is not a pure vertical step. Instead, it is likely a vertical step with a gradual increase that comes immediately after the step.

Consider the effect of dimers that dissociate in the acceleration region. After the instant the monoenergetic monomers arrive at the CEM, the monomers produced by dimer dissociation in the acceleration region begin to arrive. The input signal to the amplifier is a vertical step, from the monoenergetic monomers, with a gradual increase after the step, from the broken dimers. The input signal has features from both ion populations that are readily distinguished from one another. However, due to the limited amplifier bandwidth, the transition from the vertical step to the gradual increase is obscured in the amplifier output signal, as shown in Fig. 17(b). This means that the signal features from the two populations cannot be distinguished from one another within a particular time interval, Δt, after the monoenergetic monomer arrival time. At a later time, $t_1 = t_0 + \Delta t$, the amplifier response recovers and the output signal is proportional to the input signal. The measured TOF signal after t_1 is reliable for dissociation rate analysis.

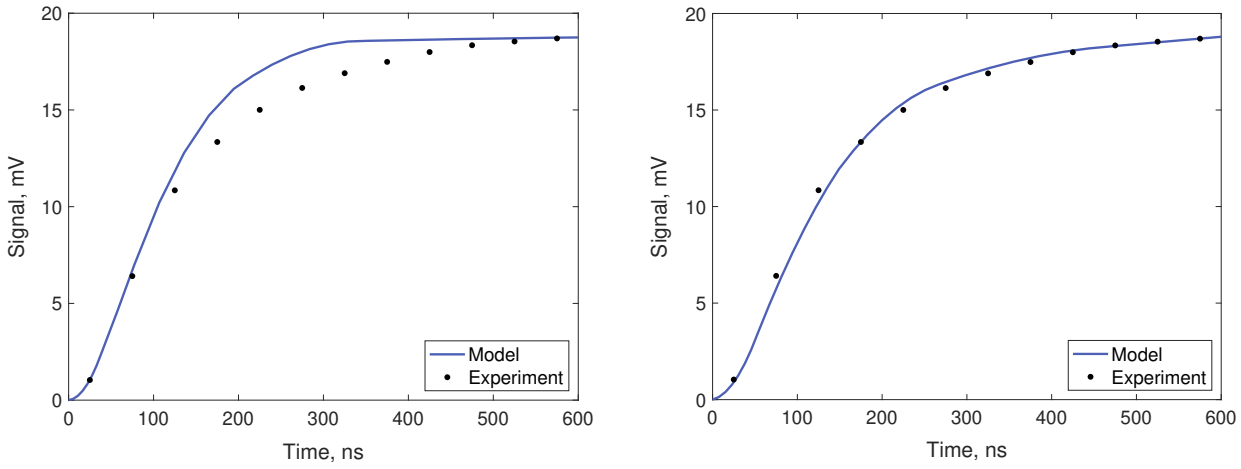

Fig. 17 Measured TOF data for the monoenergetic monomer step (V_0 = 2020V, T = 70°C) compared with amplifier model outputs for: (a) vertical step input signal (b) vertical step with exponential decay input signal.

This time, t_1, is the flight time of a broken dimer that dissociates at a particular location within the acceleration region, call this z_1. Therefore, the amplifier bandwidth places a limitation on where in the acceleration region dissociation rates can be determined. Dissociation that occurs closer to the emission site than the point z_1 cannot be determined using the TOF data. As an example, assume $\Delta t = 300$ ns. For the experimental measurement considered in this section, the point z_1 corresponds to an electric potential of 1875 V, which is approximately 93% of the source potential. The point also corresponds to a distance from the emission site of 10.7 micrometers and a field strength of 1.0×10^7 V/m. In order to determine the dissociation rates at electric field strengths greater than 10^7 V/m, improvements to the experimental instrumentation must be made.

Adjustments to the TOF measurement electronics should be made to increase the amplifier bandwidth. The Channeltron voltage should be increased such that the output signal approaches saturation. The maximum output current of the CEM used in this work is approximately 10 μA. With this as an input signal, an amplifier gain of 10^4 is required to produce a 100 mV output signal, which is the minimum recommended amplitude for a sufficient signal-to-noise ratio. The AD8067 circuit gain should be set to 25, resulting in a bandwidth in excess of 10 MHz, which corresponds to a rise time of 35 ns [27]. The shunt resistor can be set to 400 Ω to achieve a net amplifier gain of 10^4. If the input capacitance can be reduced to 40 pF by reducing cable lengths, the RC circuit bandwidth would be approximately 10 MHz. The 10% to 90% rise time for a SPICE model of this new design is 40 ns. Following similar analysis as in the previous paragraph, the maximum electric field strength that can be proved for the new amplifier design is 1.8×10^7 V/m, which corresponds to $\phi_{br} = 0.986\phi_0$.

In addition to modifying the TOF measurement electronics, the TOF signal can be stretched out over time by reducing the source potential and increasing the flight distance. This, in effect, reduces the minimum required amplifier bandwidth. The flight time of any ion varies linearly with the flight distance, since $t_f = L/v$. Increasing the flight distance will scale the TOF signal linearly in time by a factor of L'/L, where L is the original flight length and L' is the new flight length. By Eq. 8, the flight time of any broken ion varies with the inverse square root of the source potential. Decreasing the source potential will scale the TOF signal linearly in time by a factor of $\sqrt{\phi_0/\phi_0'}$, where ϕ_0 is the original source potential and ϕ_0' is the new source potential. If the flight length could be lengthened to 1 m and if the source potential could be reduced to 1000 V, then the dissociation rates could be determined up to $\phi_{br} = 0.961\phi_0$ with the old amplifier design. With the new amplifier design, the dissociation rates could be determined up to $\phi_{br} = 0.993\phi_0$.

B. Derivation of the Broken Ion Velocity

A parent ion cluster of mass m_{pi} and charge q is evaporated from the liquid meniscus with initial speed v_0. The electric potential at the meniscus is ϕ_0, so the initial mechanical energy of the parent ion, $E_{pi,0}$ is:

$$E_{pi,0} = \frac{1}{2} m_{pi} {v_0}^2 + q\phi_0 \tag{15}$$

The parent ion cluster breaks up at a particular location within the acceleration region where the electric potential is ϕ_{br}. The speed of the parent ion at this location is v_{br}. Thus the mechanical energy of the parent ion immediately before breaking up, $E_{pi,br}$ is:

$$E_{pi,br} = \frac{1}{2} m_{pi} {v_{br}}^2 + q\phi_{br} \tag{16}$$

If there is no work done on the parent ion by non-conservative forces and there are no other mechanisms for energy loss, the mechanical energy of the parent ion will remain constant along its trajectory: $E_{pi,0} = E_{pi,br}$. Thus the speed of the parent ion immediately before breaking up is:

$$v_{br} = \sqrt{{v_0}^2 + \frac{2q}{m_{pi}} \left(\phi_0 - \phi_{br}\right)} \tag{17}$$

The parent ion cluster breaks up into a broken ion, of mass m_{bi} and charge q, and a neutral cluster. The broken ion has an initial speed of v_{br}. Thus the mechanical energy of the broken ion immediately after being created is:

$$E_{bi,br} = \frac{1}{2} m_{bi} {v_{br}}^2 + q\phi_{br} \tag{18}$$

The broken ion travels to the exit of the thruster, without dissociating. The mechanical energy of the broken ion at the thruster exit, $E_{br,f}$, is:

$$E_{bi,f} = \frac{1}{2} m_{bi} {v_{bi}}^2 \tag{19}$$

Note that the electric potential at the thruster exit is zero. If there is no work done on the broken ion by non-conservative forces and there are no other mechanisms for energy loss, the mechanical energy of the broken ion will remain constant along its trajectory: $E_{bi,\,br} = E_{bi,\,f}$. Thus the speed of the broken ion at the thruster exit is:

$$v_{bi} = \sqrt{{v_0}^2 + \frac{2q}{m_{pi}}\left(\phi_0 - \phi_{br}\right) + \frac{2q}{m_{bi}}\phi_{br}} \tag{20}$$

Acknowledgments

This work was supported by a NASA Space Technology Research Fellowship, the Air Force Research Laboratory, and other government agencies. The author thanks members of the MIT Space Propulsion Lab for their contributions. The author would also like to thank Middlebury College for travel funding support.

References

[1] Poghosyan, A., and Golkar, A., "Cubesat evolution: Analyzing CubeSat capabilities for conducting science missions," *Progress in Aerospace Sciences*, Vol. 88, 2017, pp. 59–83. https://doi.org/10.1016/j.paerosci.2016.11.002.

[2] Khayms, V., "Advanced Propulsion for Microsatellites," Ph.D. thesis, Massachusetts Institute of Technology, Cambridge, MA, Jun. 2000.

[3] Lozano, P., and Martínez-Sánchez, M., "Ionic Liquid Ion Sources: Characterization of Externally Wetted Emitters," *Journal Of Colloid And Interface Science*, Vol. 282, No. 2, 2004, pp. 415–421. https://doi.org/10.1016/j.jcis.2004.08.132.

[4] Krejci, D., Mier-Hicks, F., Thomas, R., Haag, T., and Lozano, P., "Emission characteristics of passively fed electrospray microthrusters with propellant reservoirs," *Journal of Spacecraft and Rockets*, Vol. 54, No. 2, 2017, pp. 447–458. https://doi.org/10.2514/1.A33531.

[5] Lozano, P., and Martínez-Sánchez, M., "Energy properties of an EMI-Im ionic liquid ion source," *Journal of Physics D - Applied Physics*, Vol. 39, No. 1, 2006, pp. 126–134. https://doi.org/10.1088/0022-3727/39/1/020.

[6] Fedkiw, T., and Lozano, P., "Development and characterization of an iodine field emission ion source for focused ion beam applications," *Journal of Vacuum Science and Technology: Part B - Microelectronics and Nanometer Structures*, Vol. 27, No. 6, 2009, pp. 2648–2653. https://doi.org/10.1116/1.3253604.

[7] Chiu, Y., Austin, B., Dressler, R., Levandier, P., Murrary, P., Lozano, P., and Martínez-Sánchez, M., "Mass spectrometric analysis of colloid thruster ion emission from selected propellants," *Journal of Propulsion and Power*, Vol. 21, No. 3, 2012, pp. 416–423. https://doi.org/10.2514/1.9690.

[8] Coles, T., and Lozano, P., "Investigating efficiency losses from solvated ion fragmentation in electrospray thruster beams," *Proc. of the 49th AIAA/ASME/SAE/ASEE Joint Propulsion Conference*, San Jose, CA, 2013.

[9] Miller, C., and Lozano, P., "Measurement of the Dissociation Rates of Ion Clusters in Ionic Liquid Ion Sources," *Applied Physics Letters*, Vol. 116, 2020, p. 254101. https://doi.org/10.1063/5.0006529.

[10] Schroeder, M., "Numerical Characterization of Fragmentation in Ionic Liquid Clusters," Master's thesis, Massachusetts Institute of Technology, Cambridge, MA, Jun. 2021.

[11] Mier-Hicks, F., and Lozano, P., "Spacecraft-Charging Characteristics Induced by the Operation of Electrospray Thrusters," *Journal Of Propulsion and Power*, Vol. 33, No. 2, 2017. https://doi.org/10.2514/1.B36292.

[12] Miller, C., "Characterization of Ion Cluster Fragmentation in Ionic Liquid Ion Sources," Ph.D. thesis, Massachusetts Institute of Technology, Cambridge, MA, Jun. 2019.

[13] Prince, B., Annesley, C., Bemish, R., Miller, S., Hause, M., and Vogelhuber, K., "A combined experimental and theoretical treatment of ionic liquid thermal dissociation," *Proc. of the AIAA Propulsion and Energy Forum*, Atlanta, GA, 2017.

[14] Prince, B., Annesley, C., Bemish, R., and Hunt, S., "Solvated ion cluster dissociation rates for ionic liquid electrospray propellants," *Proc. of the AIAA Propulsion and Energy Forum*, Indianapolis, IN, 2019.

[15] Fernández de la Mora, J., Genoni, M., Perez-Lorenzo, L. J., and Cezairli, M., "Measuring the Kinetics of Neutral Pair Evaporation from Cluster Ions of Ionic Liquid in the Drift Region of a Differential Mobility Analyzer," *Journal of Physical Chemistry A*, Vol. 123, 2020, pp. 2483–2496. https://doi.org/10.1021/acs.jpca.9b11359.

[16] Loscertales, I., and Fernández de la Mora, J., "Experiments on the kinetics of field evaporation of small ions from droplets," *Journal of Chemical Physics*, Vol. 103, No. 12, 1995, pp. 5041–5060. https://doi.org/10.1063/1.470591.

[17] Iribarne, J., and Thomson, B., "On the evaporation of small ions from charged droplets," *Journal of Chemical Physics*, Vol. 64, 1976, pp. 2287–2294. https://doi.org/10.1039/b904022f.

[18] Larriba, C., Castro, S., Fernández de la Mora, J., and Lozano, P., "Monoenergetic source of kilodalton ions from Taylor cones of ionic liquids," *Journal of Applied Physics*, Vol. 101, 2007, p. 084303. https://doi.org/10.1063/1.2717858.

[19] Castro, S., Larriba, C., Fernández de la Mora, J., Lozano, P., Sümer, S., Yoshida, Y., and Saito, G., "Effect of liquid properties on electrosprays from externally wetted ionic liquid ion sources," *Journal of Applied Physics*, Vol. 102, 2007, p. 094310. https://doi.org/10.1063/1.2802547.

[20] Prince, B., Tiruppathi, P., Bemish, R., Chiu, Y., and Maginn, E., "Molecular dynamics simulations of 1-ethyl-3-methylimidazolium bis[(trifluoromethyl)sulfonyl]imide clusters and nanodrops," *Journal of Physical Chemistry*, Vol. 119, 2014, pp. 352–368. https://doi.org/10.1021/jp507073e.

[21] Vidal, P., "Electrospray propulsion for microsatellites or cubesats," Master's thesis, Institut Supérieur de l'Aéronautique et de l'Espace, 2019.

[22] Miller, C., "On the stability of complex ions in ionic liquid ion sources," Master's thesis, Massachusetts Institute of Technology, Cambridge, MA, Jun. 2015.

[23] Lozano, P., "16.522 Lecture 18: Electrospray Propulsion," , 2015. URL https://ocw.mit.edu/courses/16-522-space-propulsion-spring-2015/pages/lecture-notes/.

[24] Gallud, X., and Lozano, P., "The emission properties, structure and stability of ionic liquid menisci undergoing electrically-assisted ion evaporation," *Journal of Fluid Mechanics*, Vol. 933, 2022, p. A43. https://doi.org/10.1017/jfm.2021.988.

[25] Coffman, C., "Electrically-assisted evaporation of charged fluids: fundamental modeling and studies on ionic liquids," Ph.D. thesis, Massachusetts Institute of Technology, Cambridge, MA, Jun. 2016.

[26] Petro, E., Gallud, X., Hampl, S., Schroeder, M., Geiger, C., and Lozano, P., "Multiscale modeling of electrospray ion emission," *Journal of Applied Physics*, Vol. 131, 2022, p. 193301. https://doi.org/10.1063/5.0065615.

[27] "AD8067 Data Sheet," , 2012. URL https://www.analog.com/media/en/technical-documentation/data-sheets/AD8067.pdf.

[28] Horowitz, P., and Hill, W., *The Art of Electronics*, 3rd ed., Cambridge University Press, 2015.